Mathematical modelling of the fibre laser surface processing of a zirconia engineering ceramic by means of three-dimensional finite-element analysis

P P Shukla* and **J Lawrence**
Optical Engineering Department, Wolfson School of Mechanical and Manufacturing Engineering, Loughborough University, Leicestershire, UK

The manuscript was received on 19 April 2010 and was accepted after revision for publication on 11 August 2010.

DOI: 10.1243/09544062JMES2434

Abstract: The thermal effects of fibre laser surface treatment on a ZrO_2 engineering ceramic were studied using a computational finite-element model (FEM). Temperature increases on the surface and the bulk of the ZrO_2 during the fibre laser processing were measured using an infra-red thermometer and specifically located thermocouples. The results showed an error of 5 per cent with the surface and 18 per cent within the bulk of the ZrO_2 when comparing the experimental readings with those of the FEM. The FEM revealed a relationship between the traverse speed, power density, time, depth, and the temperature during various stages of the fibre laser surface treatment of the ZrO_2. By utilizing data obtained from a thermogravimetry-differential scanning calorimetry (TG-DSC), the FEM predictions of the temperature distribution were used to map phase transformations and significant events occurring during the fibre laser surface treatment of the ZrO_2. The mapping revealed that the fibre laser surface treatment generally resulted in a phase transformation of the ZrO_2 at various temperatures changes as further shown in the article.

Keywords: fibre laser, surface processing, ZrO_2 engineering ceramics, finite-element modelling, phase transformation, Unigraphics (Nastran NX 5.0)

1 INTRODUCTION

Laser interaction with any material is a complex phenomenon and this is especially so with engineering ceramics since the laser process involves multi-factors such as power density, traverse speed, instantaneous heating, ablation, rapid cooling, and solidification. To analyse such events, thermal analysis by means of employing the experimental, analytical, and computation approaches can be useful to investigate the laser–ceramic surface interaction.

Previous research by several workers has revealed ways of predicting and calculating the surface and the bulk temperature of various laser processing methods by using numerical means. Cline and Anthony [**1**] conducted one of the first investigations to determine the temperature profiles of a metallic alloy during CO_2 laser processing. They presented an analytical model using the Greens' function for a Gaussian laser beam traversing at a constant velocity. Lax [**2**, **3**] investigated a one-dimensional (1D) numerical integral of a solid material by the temperature rise during an onset of a Gaussian laser beam when applying a steady-state solution and by taking in account the constant and the temperature-dependent thermo-physical properties for the solid. Nissim *et al.* [**4**] also used Greens' function to calculate temperature profiles of an elliptical laser beam during annealing of a silicon gallium arsenide (semiconductor). Their results showed that with prior knowledge of the thermal conductivity, accurate temperature can be calculated and are valid for any material. Moody and Handel [**5**] as well used a continuous wave (CW) elliptical laser beam using an improved formalism of the Kirchhoff transformation to evaluate the temperature profiles on a silicon substrate. Thermal conductivity, diffusivity, and the surface reflection were considered as important functions in the analysis. Their findings showed variation in the temperature profiles within the molten, semiliquid, and solid regions.

**Correspondence author: Optical Engineering Department, Wolfson School of Mechanical and Manufacturing Engineering, Loughborough University, Loughborough, Leicestershire LE11 3TU, UK.*
email: pratik.shukla@talk21.com

Sanders [**6**] adopted the steady-state solution of a Gaussian laser beam on a solid substrate to approximate the onset of the surface temperatures. Kar and Mazumber [**7**] implemented the 3D transient heat conduction equation to generate temperature predictions as well as a finite-element model (FEM) of a Gaussian laser beam chemical vapour deposition process thereof on a pure titanium workpiece. The 3D model showed a relationship between the variation in the temperatures at fluctuating laser powers and the traverse speeds. Kar [**8**] then followed an investigation using a quasi-steady-state heat conduction model to analyse the laser heating of a solid substrate with rectangular, square, multimode, and single or multiple laser beams. Their findings presented a 3D quasi-steady-state thermal model and an approximation of the temperature spread during the laser heating with a single or multiple beams by using a rectangular spots.

Cheng and Kar [**9**] then conducted a theoretical investigation to study the densification of ZrO_2 ceramic coating processed with a moving transmission electron microscopy (TEM_{00}) mode laser beam. They produced a 3D quasi-steady-state heat conduction model by applying the Fourier integral transform method to show that the depth of the HAZ, the influence of laser power, spot size, and the processing speed on the densification of the ZrO_2 ceramic. The use of a computational and an experimental model in this study was adopted rather than a numerical model for calculating the temperature distribution because of simplicity, to obtain accuracy, and also because it is less time-consuming, particularly, with the adopting the computational FEM approach. The temperature measurement by experimental approach would also lead to achieving a realistic values as oppose to a analytical model which does not consider the physical aspects such as the heat transfer from the workpiece to the clamps or the processing table (as a second body) in contact with the test-piece. This can have a considerable effect on the temperature distribution as opposed to a finite body in space used without any constraints in the analytical models.

Experimental measurement of the processing temperatures during the laser surface treatment is rather difficult with hard, brittle engineering ceramics and often requires a lengthy and time-consuming preparation for drilling holes, positioning, and mounting the temperature sensors or thermocouples. However, this method is ideal for measuring the temperature changes in the bulk; it is not suitable for measuring the surface temperatures so pyrometers or contactless devices are also employed, as demonstrated by Zhang and Modest [**10**], Hao and Lawrence [**11**], and Ignatiev *et al.* [**12**]. Ignatiev *et al.* also stated that such measuring techniques are helpful to detect the material's phase transformation. This approach is also adopted for the investigation herein as further revealed. Temperature measurement during the laser surface treatment is important as the measured temperatures are used as an input parameter into the computational models for determining features such as deformation, bending, tensile, and compressive stresses as well as the thermal heat map and distribution of heat.

Several researches have been published on finite-element analysis (FEA) using design software such as ABAQUS and ANSYS for investigating the residual stress and thermal distribution of various laser processing technique applied on conventionally used metals and alloys. Braisted and Brockman [**13**], Yongxiang *et al.* [**14**], Ocana *et al.* [**15**], and Chen *et al.* [**16**] studied the laser surface treatment through shock peening and constructed a 3D model of the process which led to the determination of residual stress fields and surface deformation. The steady heat transfer equation to model the evaporating laser cutting process using a 3D computational FEM was studied by Kim [**17**]. Shiomi *et al.* [**18**] analysed a laser rapid prototyping of metallic powders with the aid of a FEA. Investigation of the temperature fields and the stress state during laser welding by the aid of a simulated FEM and the thermal heat map produced to improve the laser welding process was conducted by Carmingnani *et al.* [**19**], Spina *et al.* [**20**], Yilbas *et al.* [**21**], Zain-Ul-Abdein *et al.* [**22**], and Naeem *et al.* [**23**]. Much work has been conducted with modelling various laser processes with metals; however, very little work has been published with finite-element modelling of laser surface treatment of engineering ceramics.

Considerable amount of research has also been conducted within the field of phase transformation of the ZrO_2 ceramics. The phase transformation of the ZrO_2 ceramic occurs when it is exposed to increasing/decreasing or changing temperatures as stated by Zakurdaev and Huang [**24**], Luping *et al.* [**25**], and Holand and Beall [**26**]. With respect to the changing temperature being introduced during the laser surface treatment, it is important to understand the thermal effects of the laser radiation upon the crystal phases of the ZrO_2 ceramics. ZrO_2 comprises three phases within its crystal structure. Upon heating at 800 °C, the transition from monoclinic to tetragonal (M + T) phase begins to occur. At 1100 °C, the ZrO_2 ceramic fully transforms from monoclinic to the tetragonal (M − T) phase. Furthermore, the tetragonal phase (T) becomes active until 2370 °C. The reverse order takes place upon cooling of the ceramic. This was presented in the work of Garvie *et al.* [**27**], Porter and Heuer [**28**], Sergio [**29**], Zhou *et al.* [**30**], Sato and Shimada [**31**], Haraguchi *et al.* [**32**], Shackelford and Doremus [**33**], Richardson [**34**], Huang *et al.* [**35**], and Lee and Rainforth [**36**].

There are several events that take place within a ceramic during phase transformation. Previous research has shown the change in ZrO_2 phases by

introducing heat treatment such as sintering and annealing at temperatures up to 1500 °C. Sintering at temperatures up to 1500 °C would result in an increase in hardness and toughness as found by Miao *et al.* [**37**], and Nayak *et al.* [**38**]. Changes in volume, strength, and the grain boundaries depending on the concentration of the additive and the critical temperature applied were also reported by Sato *et al.* [**39**] as well as decreasing the grain size of the ZrO_2 reduces the amount of T to M phase transformation. Zhu [**40**] stated that the grain size of a 2 mol% ZrO_2 ceramic is dependent on the transformation temperature.

This research attempts to look at the underlying effects during such phase changes and how the ZrO_2 engineering ceramic is evolved from the fibre laser radiation. Thermal distribution and the change in the ZrO_2's characteristics during the fibre laser surface treatment were under investigation. This was done by performing an experimental investigation of the temperature exhibited during the fibre laser radiation within the bulk and the surface of the ZrO_2 ceramics. Consequently, mapping of the heat distributed within ZrO_2 engineering ceramics by an experimental model and by using a FEM with the aid of Unigraphics NX 5 Nastran design and simulation software by Sham [**41**] is presented herein. In addition to verification of the experimental model in comparison to the FEM, phase transformation within the ZrO_2 was speculated at various temperatures prior to, during, and after the fibre laser surface treatment of the ZrO_2 engineering ceramics. The experimental value was used as the input parameter for constructing a FEM which was then used for postulating any changes within the ZrO_2 ceramic such as phase transformations, through data obtained from a thermogravimetry-differential scanning calorimetry (TG-DSC).

2 MATHEMATICAL MODEL DEVELOPMENT OF THE FIBRE LASER SURFACE TREATMENT OF THE ZrO_2 CERAMIC

2.1 Thermal modelling

It is important to study the event during the fibre laser interaction with the ZrO_2 ceramic. The fibre laser with a given power density and a constant traverse speed (see section 3.2) is passed on the top surface of the ceramic. During this time, the laser energy is absorbed by the ceramic and to about 90 per cent as reported by Zhang and Modest [**10**]. The absorbed light in form of heat causes a degree of surface heating, which leads to a degree of melting, followed by some level of ablation through vaporization and finally solidifies during its cooling process to ambient temperatures. Phase changes during such events also occur at certain temperature gradients as mentioned earlier in this study. Furthermore, an analytical solution as presented in equation (1) onwards can be adopted to evaluate an analytical model Q4

$$\frac{\partial^2(k\theta)}{\partial x^2} + \frac{\partial^2(k\theta)}{\partial y^2} + \frac{\partial^2(k\theta)}{\partial z^2} + qb = \rho c_p \frac{\partial \theta}{\partial t} \tag{1}$$

and θ is the temperature and k_{ij} are the conductivity coefficient. The variables ρ, c_p, and q_b are mass density, the specific heat, and the rate of heat generation per unit volume. The thermal energy acting on the surface of the ZrO_2 ceramic due to convection to the environment is governed by

$$q = -h(\theta - \theta^0) \tag{2}$$

where q is the heat energy across the surface, h is a reference film coefficient, θ is the temperature at this point on the surface, and θ^0 is a reference temperature value. The thermal energy on the ZrO_2 ceramic is due to radiation to the environment and is governed by

$$q = A[(\theta - \theta^Z)^4 - (\theta^0 - \theta^Z)^4] \tag{3}$$

where q is the thermal energy across the surface of the ZrO_2 ceramic, A is the radiation constant, θ is the temperature at this point on the surface, θ^0 is an ambient temperature value, and θ^Z is the value of absolute zero on the temperature scale being used. Therefore, the radiation constant is defined as

$$A = \varepsilon\sigma \tag{4}$$

where ε is the emissivity of the surface and the σ is the Stefan–Boltzmann constant. In a situation where phase change occurs, particularly so for a pure substance, the following boundary conditions of Rolph and Bathe [**42**] is applied at the phase transition interface at the solid–liquid interface

$$\theta = \theta_f \tag{5}$$

$$\Delta q_s \, \mathrm{d}S = -\rho L \, \mathrm{d}V/\mathrm{d}t \tag{6}$$

where θ_f, ρ, and L are the phase change temperatures, mass density, and latent heat per unit mass of the material undergoing phase change, and V is the volume. The heat is absorbed at a rate proportional to the volumetric rate of conversion of the material, $\mathrm{d}V/\mathrm{d}t$, at the solid–liquid interface as stated by equation (7). Q5 The heat must also be balanced by the heat flow, Δq_s, from the interface. The –ve sign is used for a situation where absorption of heat during melting occurs. The steps to construct the FEM by using a computational method of steady-state solution are further presented with its 3D geometry.

2.2 FEM development

A FEM was constructed using the Unigraphics NX 5.0 Nastran designing software. The model presents the thermal distribution of the fibre laser-radiated heat

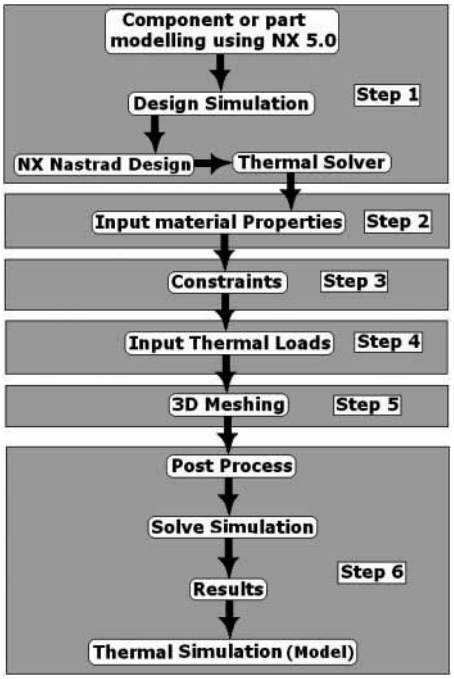

Fig. 1 A schematic diagram of the steps taken to construct the FEM

which is compared to the experimental heat distribution model to investigate if there is a correlation between the two methods. The steps taken for the FEA are illustrated in Fig. 1.

The component part was first designed which represented the experimental workpiece (see Fig. 2). It comprised a diameter of 3 mm diameter blind hole with a depth of 100 μm, equivalent to the footprint of the fibre laser beam. A depth of 100 μm was assigned for the blind hole as it was found from previous investigations by Shukla and Lawrence [**43**, **44**] that the average laser beam penetration on the ceramic was about 100 μm in depth. It was necessary to introduce the blind hole to the model to assign a heat load acting on the workpiece as opposed to assigning the laser beam as a heat load since the laser beam is not a solid object and does not have the required physical properties for the model to function correctly. This also helped to minimize the computational time and the model complexity during the simulation.

The second step to construct the model was to assign the material properties. However, the user must ensure that the correct software functions are selected, namely the design simulation followed by the NX Nastrad design and the thermal solver. The material properties are presented in Table 1 and then assigned to the workpiece. Young's modulus, Poisson's ratio, shear modulus, thermal expansion coefficient, and the thermal conductivity are predominant properties directly affecting the model and, hence, were assigned in all three X, Y, and Z directions using the orthotropic material function of the NX Nastrad design (thermal solver). This was because the characteristic of the ceramic does not remain the same in all axes of its orientations as shown in the previous research by Shukla and Lawrence [**43**].

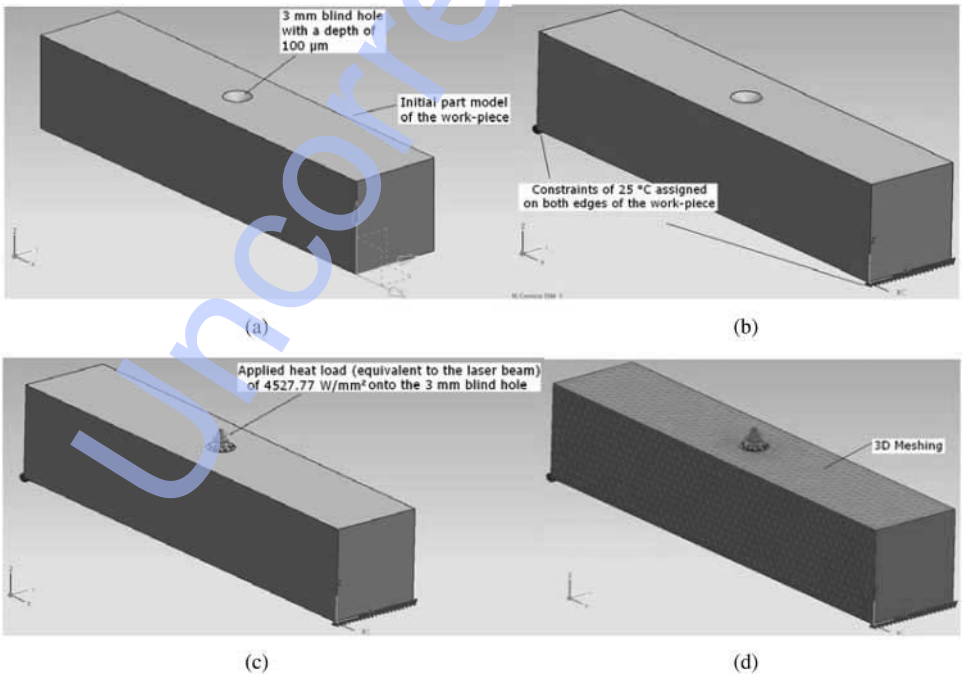

Fig. 2 (a) Screen shot images of the part design showing a 3 mm diameter blind hole at a depth of 100 μm, (b) the thermal constraint of 25 °C applied on both edges to the workpiece, (c) application of the heat load to the workpiece in form of the laser beam, and (d) an image of the full 3D mesh showing the assigned heat load to the ZrO_2 engineering ceramic

Table 1 Input of the properties assigned to the ZrO_2 engineering ceramic to construct the FEM

Q19

Material properties	Value
Mass density	6050 kg/m^3
Reference temperature	25 °C
Specific heat	425 J/(kg °C)
Young's modulus	280 000 MPa
Poisson's ratio	0.28
Shear modulus	55 000 MPa
Thermal expansion coefficient	7 × 10–6/°C
Thermal conductivity	1.85 W/(m °C)
Thermal capacity	400 J/(kg °C)

After assigning the material properties, the third step of the FEA was to give constraints (see Fig. 1) to the workpiece or to set the boundary conditions. The constraint is in form of a thermal constraint and is assigned to the workpiece in positions where the sample is connected to another body (i.e. mounted to the processing table by using putty). Putty was used since mechanical clampings are not always ideal for holding hard brittle ceramics due to the risk of as inducing a mechanical tensile stress which often leads to propagation of fractures. Furthermore, the use of putty provided a firm fixation and avoided vibrations when the working table was in motion during the fibre laser processing. A thermal constraint of 25 °C was applied to the positions shown in Fig. 2(c) on both edges of the workpiece. This meant that the workpiece was held firm in those positions and was in contact with another body during the fibre laser processing. The temperature of the thermal constraint was applied at an atmospheric temperature of 25 °C. Step four of the FEA involved applying a heat load to the workpiece. This is where a heat load of 2483 °C found from the experimental work was applied on the 3 mm diameter blind hole (see Fig. 2(c)) on the workpiece at the laser power density of 4527.77 W/mm^2. This was the maximum power density induced by the 3 mm diameter beam of the fibre laser. The surface of the ZrO_2 was assigned a view factor of 1. This is the amount of or heat being passed on from one surface to another; in this case, the thermal energy radiated by the laser beam was only being passed onto one surface during the heat transfer as described by Cengel and Turner [**45**]. Absorption of 90 per cent was assigned to the model by taking in consideration of the absorption values found in a previous investigation by Zhang and Modest [**10**]. An emissivity of 0.40 was used as it is a typical value for all ceramics.

Once a thermal load was applied the FEM is then ready to be meshed. Furthermore, a fine 3D mesh of tetrahedral using ten nodes, with an overall element size of 1 mm, was created on the workpiece as is presented in Fig. 2(d). The final step of the FEA is to create a simulation using the post-processing function of the NX 5.0 Nastran software. This generated a solution from the input data and produced a simulation in form of a FEM which was also animated to investigate the distribution of heat prior to, during, and after the laser process.

3 EXPERIMENTAL TECHNIQUES AND ANALYSIS

3.1 Experimental material

The material used for the experimentation was cold isostatic pressed ZrO_2 with 95 per cent ZrO_2 and 5 per cent yttria (Tensky International Company Limited). Each test piece was obtained in a bulk of 10 × 10 × 50 mm^3 with the as-received surface roughness of 1.58 μm (*Ra*). This was to reduce the laser beam reflection as the well-polished shinier surfaces of the ceramic would reduce beam absorption. The experiments were conducted in an ambient condition at a known temperature (25 °C). All surfaces of the ZrO_2 to be treated were marked with black ink prior to the laser treatment to enhance the absorption and allow the laser beam to further penetrate into the surface.

3.2 Fibre laser treatment

A 200 W fibre laser (SP-200c-002; SPI Limited) emitting a CW mode beam at a wavelength of 1.075 μm was used for this work (see Fig. 3). The focal position was kept to 20 mm above the workpiece to obtain a 3 mm spot size. The processing gas used was compressed air as well as ambient air supplied at a flow rate of 25 l/min. Programming of the laser was conducted using the SPI software which integrated with the laser system. A 50 mm line was programmed using numerical control programming as a potential beam path which was transferred by .dxf file. To obtain an operating window, trials were conducted at the fixed spot size of 3 mm and by varying the power between 75 and 200 W and varying the traverse speed between 25 and 500 mm/min. From these trials, it was found that 137.5–143.25 W at 100 mm/min were the ideal laser parameter to use in terms of achieving a crack-free surface.

3.3 Temperature measurements

3.3.1 Infra-red thermometer

The surface processing temperature was measured by using a portable infra-red thermometer (Cyclops 100 B; Land instruments International Limited). The device was bolted on a tripod and positioned 1 m away from the processing area (see Fig. 3). The infra-red thermometer was then aligned with the workpiece by means of a He–Ne beam of the fibre laser as indicated in position 5 in Fig. 4. Thereafter, the laser beam was switched on for the surface treatment to take place. The infra-red thermometer was then switched

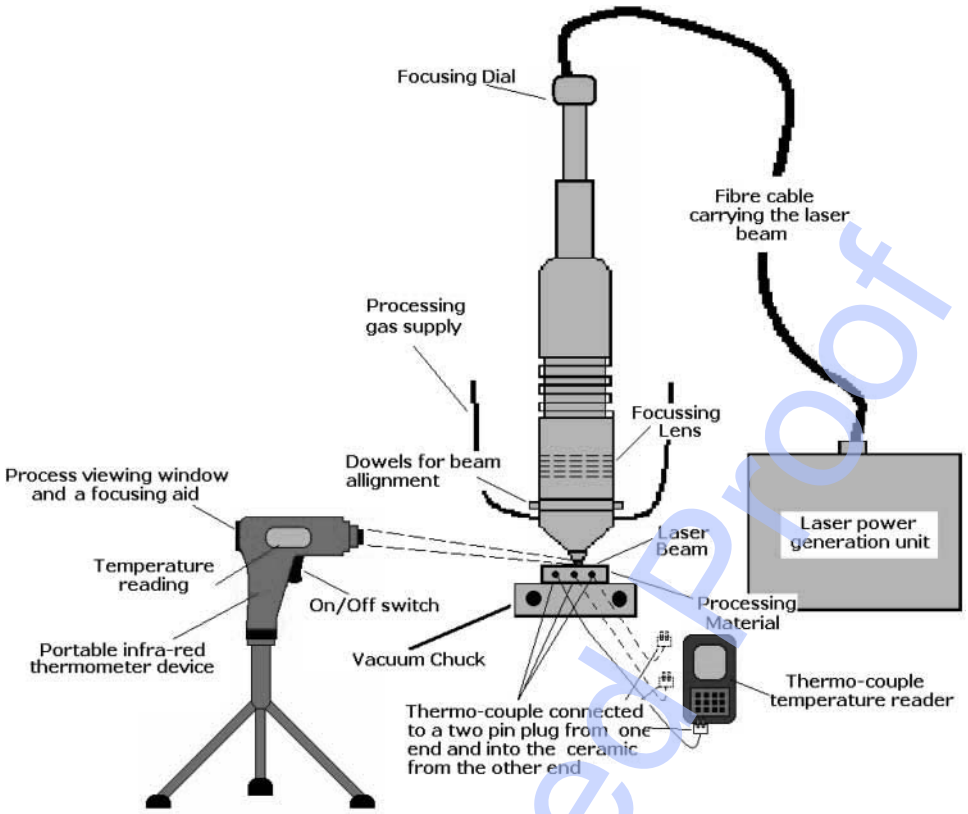

Fig. 3 A schematic diagram of the experimental set-up of the fibre laser processing of the ZrO_2 engineering ceramic

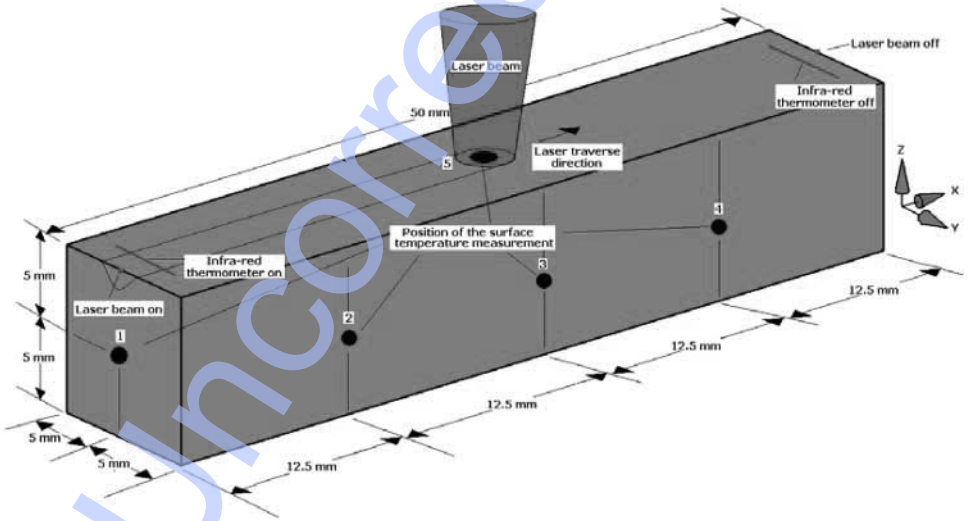

Fig. 4 A schematic diagram of the positions used to measure the surface temperature of the ZrO_2 engineering ceramic during the fibre laser processing

on shortly after and followed the laser ceramic interaction as the laser processing began. The infra-red thermometer was switched off before the fibre laser processing was completed (see Fig. 4). This procedure was adopted for every measurement that was taken for the experiment which allowed an average temperature to maintain closer to the real temperature of the processing area. However, it was important that the operator constantly monitored the processing area through the viewing window of the lens of the infra-red thermometer, whereby the traversing laser beam was followed in order to accurately measure the temperature during the laser processing. The temperature measurement was conducted on five different areas

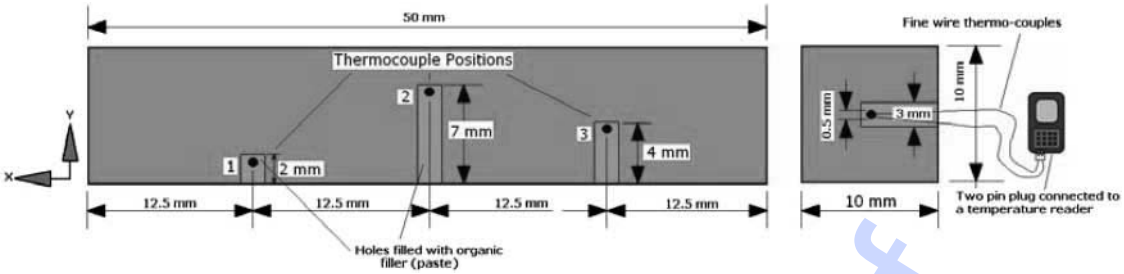

Fig. 5 A schematic diagram of the mounting position of the thermocouples into the ZrO_2 engineering ceramic workpiece during the fibre laser surface radiation

of the surface of the ceramic workpiece as indicated in Fig. 3. The measurement on the surface was conducted as the beam traversed on the surface of the workpiece. Each area was measured in one pass of the laser beam. The average reading of the temperature was taken from five passes of the laser beam executed on five samples which enabled to produce consistent values of the temperature measurement.

3.3.2 Digital temperature reader

The bulk temperature measurement was taken using a precision fine wire (0.20 mm diameter × 152 mm in length), R-type, thermocouples, capable of reading up to 2300 °C (P13R, Omega Instruments Limited) and were precisely mounted at various positions within the bulk of the sample as illustrated in Fig. 5. Each of the fine wire thermocouples set was wired to a two-pin plug which connected to a digital temperature reader (N9002-Thermometer; Comark Limited) for receiving the feedback in for of a temperature reading. Three holes were drilled into the ceramic using the ultrasonic drilling method, after which the tip of the thermocouples were mounted into the holes at 3, 6, 8 mm from the surface (see Fig. 5). The holes were then filled using filler (paste) made of organic-type material that is stable during high-temperature processing. This assured firm fixation for the thermocouples during the laser processing. Measurement was taken in three different passes of the laser treatment as one pass could only measure the temperature from a single set of thermocouple positioned in a single hole. A new sample was used with each pass of the fibre laser and five identical readings were recorded for each of the positioned hole to achieve consistency in the bulk temperature measurement.

3.4 TG-DSC analysis

TG-DSC analysis (1500 DSC; Stanton Redcroft Limited) was conducted on the as-received and fibre laser-treated ZrO_2 samples. The average surface area of the samples was approximately 2 mm^2 and the mass was 29.45 mg. The samples were placed into an Al_2O_3 crucible and N_2 was used as a purge gas at 50 ml/min. Once in place, the samples were heated up to 1500 °C at a rate of 10 °C/min to measure the mass flow as the temperature increased. The samples were then cooled to ambient temperature at the same rate using the same parameters to measure the mass flow as the temperature reduced. The heat flow through the as-received and fibre laser-treated samples was recorded for any changes during the heating and cooling cycles and is shown in Fig. 15. From this recording it was then possible to identify specific phase events that occur in the ZrO_2 during heating at what temperature these events take place. Q7

4 RESULTS AND DISCUSSION

4.1 Experimental temperature readings

The average temperatures found on the surface after five passes of the fibre laser are presented in Fig. 6(a), the surface temperature, and in Fig. 6(b), the bulk temperature of the ZrO_2 ceramic. At the laser–ceramic interface the surface temperature was found to be 2483 °C. This is close to the manufacturer's specification of the melting temperatures (2550 °C) in comparison. The difference between the two readings was 2.5 per cent which could be justified by the accuracy and the operator error that may have occurred during experimentation. This result is also in good agreement with that of a previous investigation where it was found that the laser surface treatment resulted to some degree of melting of the top (near) surface layer as found by Shukla and Lawrence [**43**]. The surface temperature on the side of the sample (away) from the laser-treated zone was found to be much lower than the melting temperature which would obviously be high due to the heat transferring through the bulk of the ceramic. Interestingly, the temperatures reading should result to being stable throughout one surface plane; however, this was not the case as the difference between position 2, 3, and 4 was sufficiently large (251 °C).

The temperature measurements taken from using the thermocouples within the bulk of the ZrO_2 ceramic

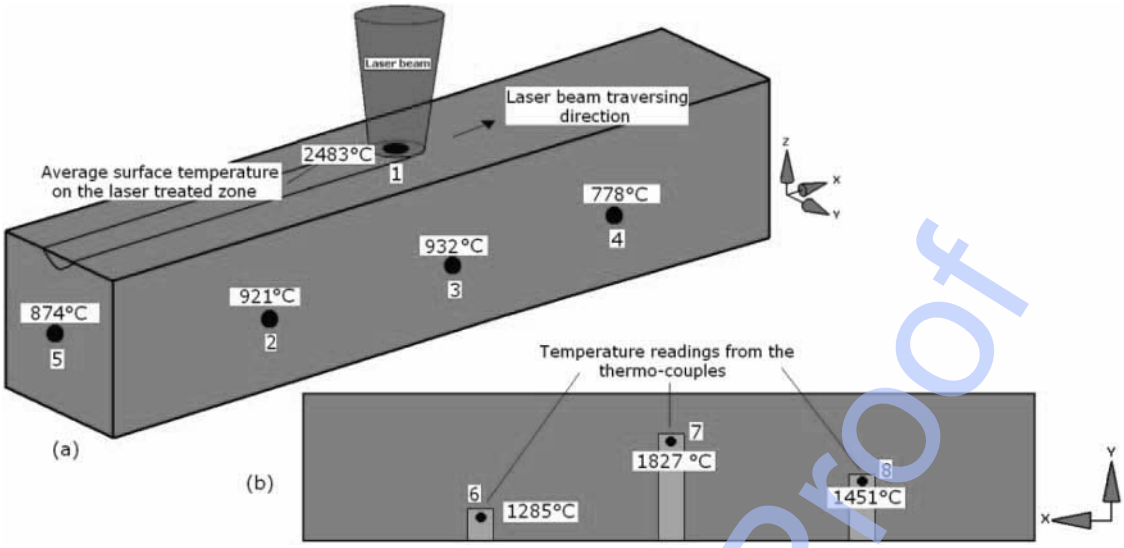

Q18 **Fig. 6** (a) Schematic of the surface temperature reading and (b) the bulk temperature of the ZrO_2 engineering ceramic

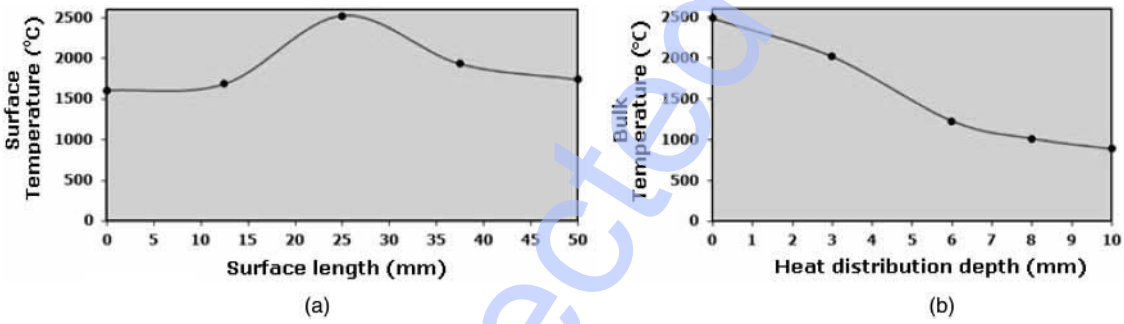

Q18 **Fig. 7** (a) Experimental temperature distribution over the surface length and (b) the temperature distribution through the bulk of the fibre laser-processed ZrO_2 engineering ceramic

are presented in Fig. 6(b). The average bulk temperature after five readings in position 6, 7, and 8 were
Q8 1285, 1827, and 1451 °C, respectively. This result agrees with the surface temperature presented in Fig. 6(a) that 3 mm below the surface due to the heat transfer; the temperature is above 400 °C lower. At 6 mm below the surface, the measured temperature was considerably lower (1225 °C). In this position, the temperature has begun to decrease as the heat was distributed throughout the surface. Moreover, the temperature at 8 mm below the surface was 1007 °C as the heat was passed on from the bulk of the ceramic to the surface.

In Figs 7(a) and (b), both of the graphs are constructed from the experimental values found. This was for a situation where the fibre laser was incident at 25 mm length (centre) from the edge of the ZrO_2 ceramic. The distribution of heat is presented in Fig. 7(a), which illustrates the surface temperature over the length of the ZrO_2 sample at 25 mm. At the length of 0 mm the experimental temperature was instantaneously ramped up to 1604 °C and gradually increases as it come closer to the incident beam. The peak temperature found was 2483 °C at 25 mm length (centre of the workpiece) of the focused laser beam upon the ZrO_2 test piece. The temperature reduced to 1935 °C at 37.5 mm in length and was recorded at 1739 °C at the edge of the sample at 50 mm.

The graph in Fig. 7(b) presents the experimental temperatures obtained in the bulk of the ceramic particularly at 3, 6, and 8 mm. Temperatures at various other positions can also be calculated from these three values as shown in Fig. 7(b). In general, the curve in Fig. 7(b) has declined due to the reduction of the temperature through the bulk of the ceramic. The temperature is reduced from 2483 °C at the depth of 0 mm (surface) to 2015 °C at 3 mm, 1225 °C at 6 mm, and 1007 °C at 8 mm depth. From this, the temperature at the depth of 10 mm can be predicted as shown in Fig. 7(b). The experimental investigation would now be used as a base to construct the FEM. The results found herein are also compared to the FEM for validation and confirmation of the level of accuracy or error in the temperature measurements in this study.

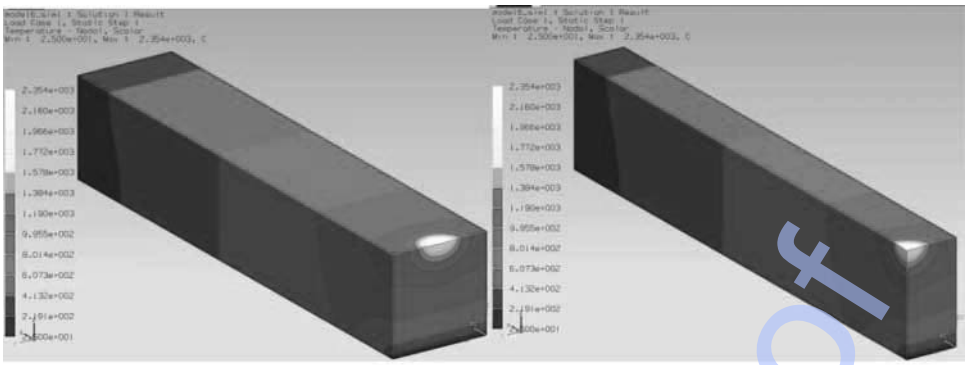

Q18 **Fig. 8** (a) FEM of the heat distribution of the fibre laser focused at 0 mm from the edge (position 1) of the ZrO_2 ceramic workpiece (start of the laser treatment) and (b) the cross-sectional view

4.2 FEM temperature reading

A FEM was constructed which revealed the surface and the bulk temperature maps by taking in account of the surface and the bulk temperatures measured from the experimentation. The surface maps are presented in Figs 8, 10, and 12. Because of the laser beam traversing as a CW beam, it is always ideal to construct the model so that it illustrates the FEA of a moving laser beam. However, in this case, a stationary spot was used for the analysis to observe the thermal radiation. The total time to cover the whole area of the sample was 30 s at a traverse speed of 100 mm/min which would cover 1.66 mm/s. In Fig. 8, the first point of contact with the ceramic and the laser beam has been demonstrated. The impact on the beam is only 1.5 mm onto the surface despite comprising a spot size of 3 mm diameter. A heat map is illustrated for this condition and is compared with the values for the experimental temperature readings that were found. It can be observed that the maximum temperature found at the laser–material interface on the FEM was 2354 °C. The temperature here was lower than the temperature from the real experimental value by 5.48 per cent. Error of the computational method within 10 per cent can be considered to be in good agreement with the experimental values. In Fig. 8(b), the laser beam is only concentrated at 50 per cent of its diameter, because it is focused on the edge of the sample (start of the laser treatment process), which enabled the cross-sectional distribution of heat to be analysed. From observing the cross-sectional heat map, it can be seen that the near to melting temperature found through the bulk of the ceramic ranges between 100 and 200 μm. This reading complied with the result of previous investigations where, a degree of surface meting has been found by Shukla and Lawrence [**43**].

From observing the results from the model in Figs 8(a) and (b), the determination of temperature distribution over the surface at various lengths and through the bulk at various depths are presented in the graphs in Figs 9(a) and (b). In this model, the incident beam at the start of the surface treatment is covering 0–1.5 mm radius. The temperature within this area as seen in Fig. 9(a) is up to 2350 °C. During this time, the temperature distribution over the rest of the surface is lower. This is due to the heat transfer taking effect over the surface. At 25 mm in the centre of the workpiece, the temperature was up to 710 °C and at 50 mm (edge of the sample), the temperature was much lower (120 °C). The result of the FEM at this position appears

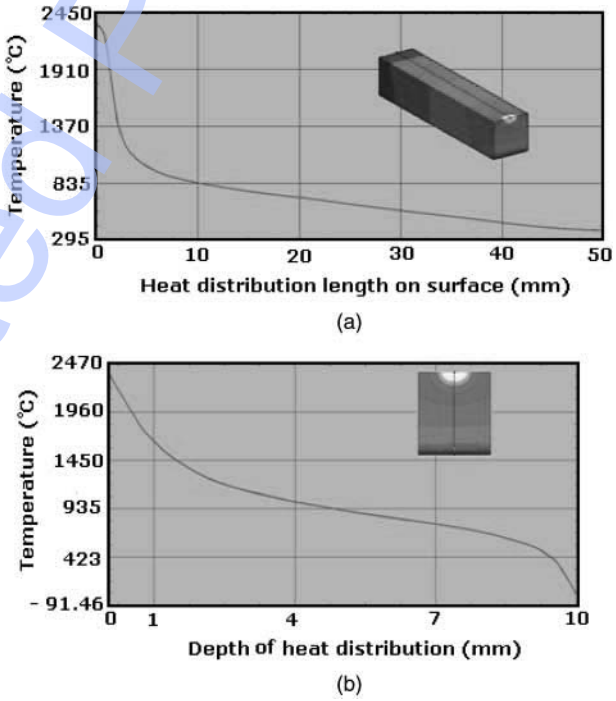

Fig. 9 Temperature curves from the FEM of the initial stage at 0 mm from the edge (position 1) of the fibre laser irradiation of the ZrO_2 ceramic for (a) the heat distribution over the length of the sample and (b) the heat distribution through the depth of the sample

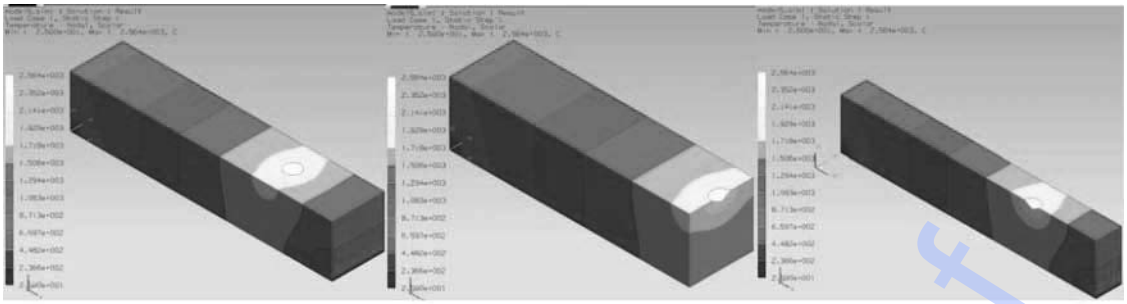

Q18 **Fig. 10** (a) FEM of the heat distribution of the fibre laser focused at 12.5 mm from the edge (position 2) of the ZrO_2 engineering ceramic and (b and c) the cross-sectional view

to be in good agreement with that of the experimental result. However, from observing the depth of the distribution from the model in Fig. 9(b), the surface temperature at 0 mm is 2350 °C and reduces to 1190 °C at the depth of 2 mm, 1000 °C at 4 mm, 794 °C at 7 mm, and finally to 25 °C at 10 mm (room temperature).

The FEM in Figs 10(a) to (c) and 7(c) all showed that the temperature pattern was somewhat different from that of the one found at the start of the laser treatment (see Figs 8 and 9) as the average heat input began to increase over the total surface area of the ZrO_2 ceramic. Despite the effect of surface melting during the laser interaction and the rapid cooling effect taking place, the temperature at the laser-radiated zone has increased on the surface and through the bulk as presented in the graph in Figs 11(a) and 7(b).

The traversing laser beam is paused in time at 12.5 mm from the edge in order to show the effects at that position. At 12.5 mm as presented the temperature is at its highest (2564 °C) (see Fig. 11). Gradually, the temperature begins to decrease to 1348 °C at 25 mm, 1018 °C at 37.5 mm, and 850 °C at 50 mm. The temperature through the bulk has increased in comparison to the bulk temperature during the start of the fibre laser treatment due to the increased in time that the laser beam has spent on the ceramic which would have caused a sufficient level of heat to be produced. From melting temperatures at 0 mm (surface), the temperature reduces to 1675 °C through the bulk during the laser–ceramic interaction at 12.5 mm in length after the start of the treatment.

The illustrations in Figs 12(a) to (c) show the FEM of the laser–ceramic interaction in the centre of the workpiece (25 mm from the edge). In this position, the distribution of heat is different to the interaction during the initial stages as previously shown. The ZrO_2 ceramic in this position is in thermal equilibrium since the temperature distribution is well balanced. At 25 mm the heat is at its peak (2587 °C) near the melting temperature of the ZrO_2 ceramic. During this time, the slope gradually increases to the highest position, maintains for 3 mm, and then declines and has

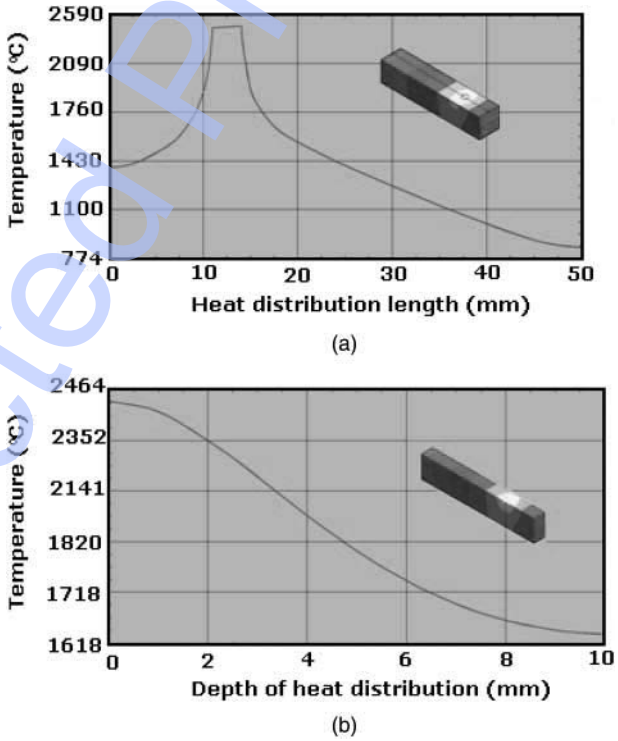

Fig. 11 Temperature curves from the FEM of the fibre laser irradiation at 12.5 mm from the edge (position 2) of the ZrO_2 engineering ceramic for (a) the heat distribution over the length of the sample and (b) the heat distribution through the depth of the sample

the opposite effect where the temperature curve is declined (Fig. 13). Q9

From this point onwards, as the laser beam traverses furthermore on to the sample, the effect of heat distribution is similar to that of the one presented in previous FEMs. The temperature distribution over the surface was similar to that of the FEM presented in Fig. 10 as well as the results obtained from the experimental model. The difference between the experimental model and the computational FEM in was up to

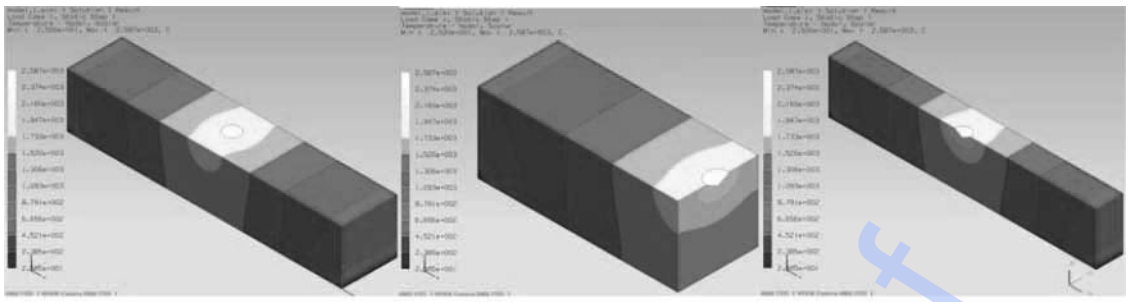

Q18 **Fig. 12** (a) FEM of the heat distribution of the fibre laser beam focused in the centre (position 3) of the ZrO_2 ceramic workpiece and (b) and (c) in the cross-section

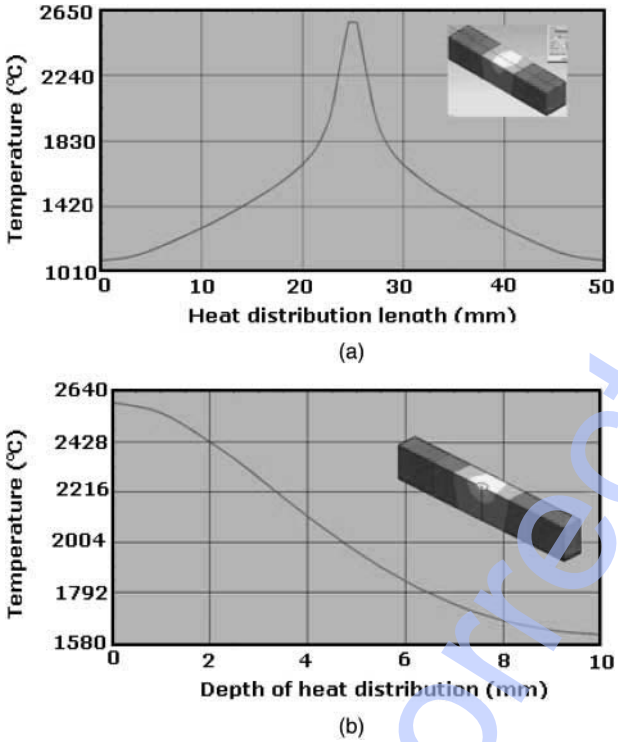

Fig. 13 Temperature curves from the FEM of the fibre laser irradiation at 25 mm from the edge (position 3) of the ZrO_2 ceramic for (a) the heat distributed over the length of the sample and (b) the heat distribution through the depth of the sample

5 per cent particularly for the temperature predictions over the surface length. The bulk readings for the two compared models were also in good agreement. However, consideration should be given to the accuracy of the thermometer device used for measuring the experimental temperature (±10 per cent) as well as the distance which the temperature measurement was taken from. The distance of the temperature measurement changes as the laser beam traverses away from the focused infra-red beam of the thermometer device (see Fig. 1) which would also cause some fluctuation in the results found.

4.3 Comparison of the experimental model and the FEM

At the laser–ceramic interface the surface temperature was found to be 2483 °C (see Fig. 6). This result is in good agreement with that of a previous investigation [**43**], where it was found that fibre laser surface treatment of ZrO_2 resulted in some degree of melting of the top (near) surface layer. Interestingly, the temperature readings would be expected to be stable throughout a plane, but this was not the case as up to 16 per cent difference in temperatures between positions 2–3 and 4–5 was observed. The difference between the two results may have resulted from the following:

(a) the error in reading the temperature resulting from the contact-less infra-red thermometer device;
(b) fluctuation in the laser power during the processing stage (although, stable output powers were recorded prior to the laser treatment);
(c) the ceramic material being somewhat inhomogeneous.

The temperature is expected to be fairly high in at the edges of the samples in position 5, (where the average temperature was measured at 1872 °C) and on the same surface plane in position 2, 3, and 4 as it is at the edge of the sample indicating that there is less area for the heat to travel which created sufficient heat at the surface. Still, the experimental surface temperature measurements agree with those of the FEA model (reference to Fig. 12) with a +10 per cent error. Further modification to the temperature measurement settings would improve the consistency in obtaining more accurate temperature readings.

The average temperatures measured within the bulk of the ZrO_2 after five readings also agree with the bulk temperatures predicted by the FEA model. At 3 mm below the surface the temperature was up to 2035 °C. The FEA by comparison gave a temperature of over 1900 °C, and agreement of just over 7 per cent. The temperature in position 8 (see Fig. 6) was found to be 1451 °C which in comparison to the FEM was 79 °C

lower, indicating an error of 5.5 per cent. Finally, at osition 6 the temperature recorded was 1285 °C, while the temperature predicted by the FEA model was 245 °C lower, a difference of 19 per cent. It is clear that the bulk material temperatures measured experimentally were slightly lower than those produced from the FEA model. This may have resulted due to three known factors:

(a) heat loss through the 3 mm holes drilled into the sample;
(b) lack of contact of the thermocouples to the material surface;
(c) the thermocouple response time. Such aspects were not taken into account by the FEA model and so the FEA results will always be higher.

4.4 Development of extended parameters from the FEM

Based on the results obtained from the FEM a range of possibilities are presented for traverse speed, power density, depth of heat distribution, temperature, and time, in relationship to one another (Fig. 14). From this, one can predict and gauge the input parameters during fibre laser processing of the ZrO_2 ceramic at various input parameters.

As with all laser processes, the results herein show that a lower traverse speed at high power density would generate high processing temperatures. This in turn would lead to a deeper distribution of the thermal energy; the effects are opposite when the processing speeds increases or the power density decreases. This is when the surface temperature is also reduced with lower penetration of the thermal energy into the bulk of the ceramic. Consideration of power density would also allow one to gauge the effect of the laser spot size as an additional parameter, since the spot is a function of the power density applied. Typically, a smaller spot size than 3 mm by using the same power input (143.25 W) would produce a much bigger power density and would further compliment the model that are presented in this study.

4.5 Phase transformation

The TG-DSC analysis is given in Fig. 15. The heating curve for the as-received ZrO_2 surface shows an exothermic peak at 50 °C and a corresponding reduction in mass flow of 8 mW, indicating a possible release of moisture. At 800 °C the small peak observed suggests a possible phase change where the mixture of M + T could have occurred. At 1290 °C a further change in the curve indicated a phase transformation of M − T. The mass flow reduced as the sample reached 1500 °C during the heating cycle. During the cooling process, mass flow was much higher and effects similar to that of the heating curve took place. At 1205 °C the curve showed an additional peak which may have occurred due to the change in the phase transformation from the T to the T + M phase.

The curve produced by the fibre laser-treated ZrO_2 sample was somewhat different to that of the as-received sample as more heat will have flowed through the bulk due to air blocks or cavities within the as-received sample, which would in turn cause a decline in the mass flow. During the heating cycle the curve produced for the fibre laser-treated ZrO_2 showed changes at 850 °C, which mark the beginning of the M + T phase change. At 1400 °C the curve showed a minor change, indicating that the T transformation had fully occurred. This is different from the effect of the as-received sample and that of a previous finding by Porter and Heuer [**28**]. A possible cause of this would be due to the ceramic changing its composition after the fibre laser treatment, hence the observed increase in mass flow. During the cooling cycle, there were no changes to be seen until 805 °C; this is a sign that the ZrO_2 had transformed back to the M state. The TG-DSC analysis only investigated changes up to 1500 °C. Since the temperatures measured experimentally and predicted from the FEA model were much higher, one can only surmise the effects beyond 1500 °C.

From observing the temperature distribution obtained experimentally and from the FEA model (see Figs 8, 10, and 12), it can be seen that the distribution of heat varies in different positions on the ZrO_2 ceramic as the fibre laser beam is frozen in one position in order to investigate the heat distribution for this study. From this, one can see that the rapid surface and the bulk heating occurs, which is followed by the rapid cooling effect which took place where the ZrO_2 is transformed from M → M + T → T → T + C during heating. It is then instantaneously transformed back from T + C → T → T + M → M.

Figure 16 presents a conventional phase diagram of the ZrO_2 ceramic with the percentage of molar content of Y_2O_3. The vertical dotted line shows that the ZrO_2 used for this work comprised of 4 mol% as stated by the manufacturer. On account of this, one can see the changes in the phases as the ZrO_2 ceramic is being heated by the fibre laser radiation. Furthermore, the phase change of the ZrO_2 can be predicted during the laser–ceramic interaction where the M + C phase ZrO_2 begins to change phase at 500 °C and transforms to a mixture of M and T phase. The M + T phase fully transforms to T at about 800 °C as presented in Fig. 16. The ZrO_2 ceramic with 4 per cent Y_2O_3 at about 1300 °C changes phase from T to T + C and then forms the C phase at about 2200 °C. Further increase in the temperature of about 2750 °C transforms the ZrO_2 into a mixture of L + C phase. Previous investigations by Shukla and Lawrence [**43**] showed that the grain boundaries of the ZrO_2 ceramic treated by the fibre laser where binding due to melting and

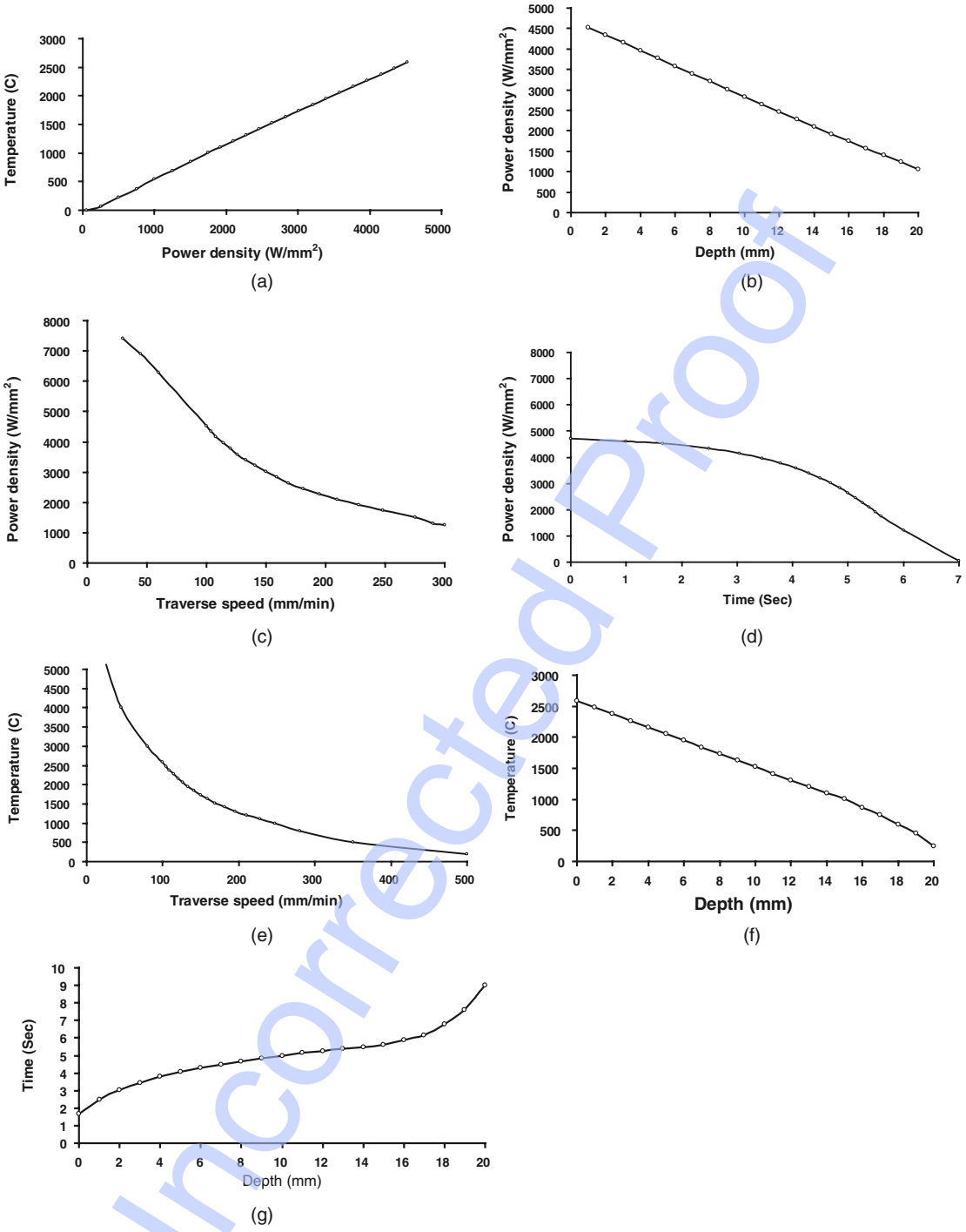

Fig. 14 Parameters obtained from the FEM showing the coloration of various parameters with one another: (a) power density versus temperature, (b) depth versus power density, (c) power density versus traverse speed, (d) power density versus time, (e) traverse speed versus temperature, (f) depth versus temperature, and (g) depth versus time

re-solidification. This indicated that the phase transformation of the ZrO_2 would be in the region of L + C state. The changes in the phase during the cooling process are reasonably symmetrical to that of the heating; however, the time it takes to heat the ceramic is much faster than the rate of cooling and so the rate of phase change is much slower during the solidification stage.

The TG-DSC results reveal the changes within the ZrO_2 ceramic during heating and cooling up to 1500 °C; however, the changes in the phase beyond 1500 °C can only be predicted from using the FEM and the experimental model as well as the phase diagram presented in Fig. 16. In addition, from observing the event of the laser material interaction, it can be stated that the ZrO_2

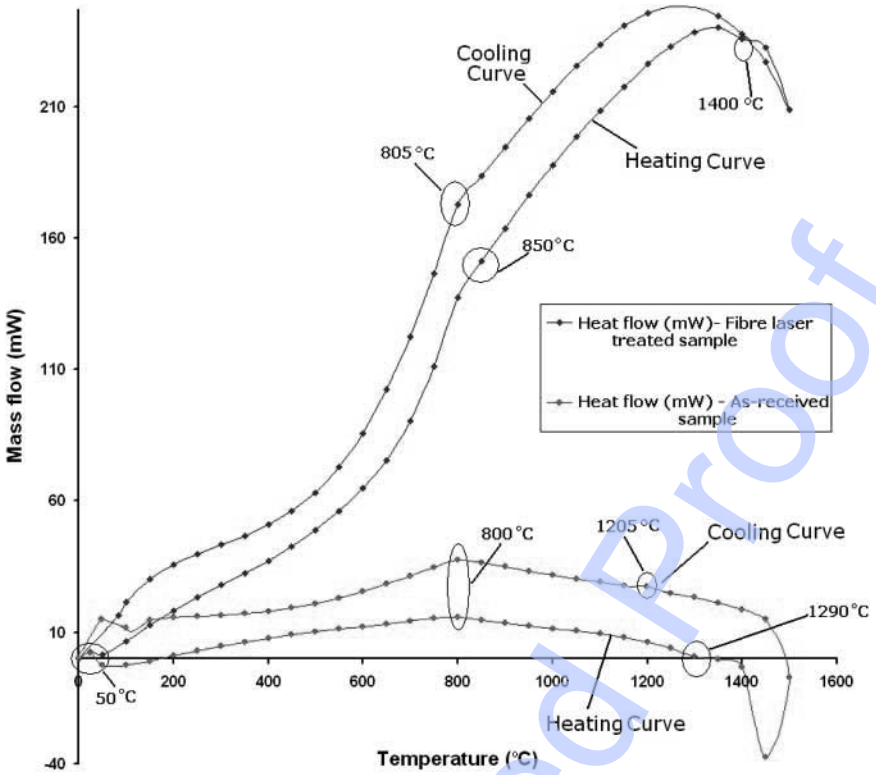

Fig. 15 TG-DSC curves for the as-received and the fibre laser-treated ZrO_2 engineering ceramic

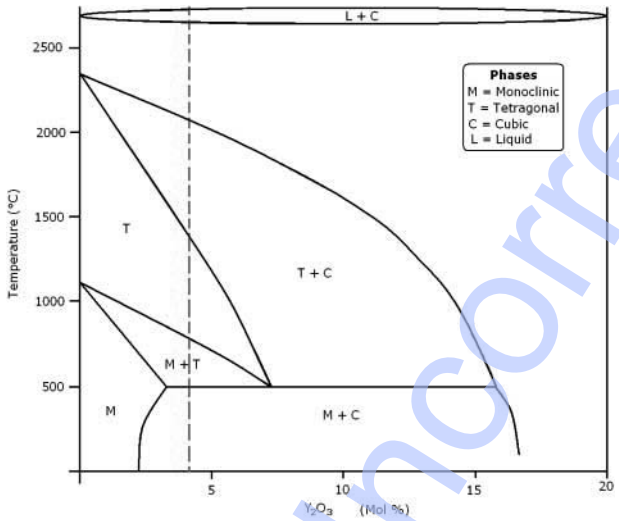

Fig. 16 A phase diagram of the ZrO_2 engineering ceramic showing the change in phase with changing temperature of 4 mol% of Y_2O_3 content within the ZrO_2 engineering ceramic used in this study

ceramic is certainly not in a thermal equilibrium. This is simply due to the feature focused laser beam executing a high power density in a small spot size which is producing a melt zone at a processing zone while the other areas of the ceramic are much cooler. This goes to show that due to the temperature difference during the fibre laser processing leads to the variations in the phase changes within the ZrO_2 where the fibre laser–ZrO_2 interaction zone maybe L + C phase while the other phases maybe of the ceramic may be a mixture of M, M + T, T, T + C, and C at the same time.

5 CONCLUSIONS

The thermal effects of the fibre laser surface treatment of a ZrO_2 engineering ceramic were modelled using an experimental model and FEM. The temperature analysis from both of the models was used to map phase changes within the ZrO_2. From both surface and the bulk temperature measurements the distribution of the temperature over the length and the depth of a ZrO_2 engineering ceramic sample during the fibre laser surface treatment was also presented and the FEA model and was verified with an overall error of +10 per cent. This is consistent over estimate of temperature by the FEA model may have resulted due to:

(a) heat loss through the 3 mm holes drilled into the sample;
(b) lack of contact of the thermocouples to the material surface;
(c) the thermocouple response time.

Such aspects were not taken in account by the FEA model and so the FEA results will always be higher. Furthermore, the FEA model expanded to show the relationship between the processing temperatures,

time, and the depth of heat distribution with parameters such as the traverse speed and power density Q11 which when correlation with one another revealed the extended range of parameter window during the fibre laser surface processing of the ZrO_2 engineering ceramic.

Data obtained from a TG-DSC analysis and the FEA model predictions were used to map the phase transformations in the ZrO_2 resulting from fibre laser surface treatment. The mapping revealed that the fibre laser surface treatment generally resulted in a phase transformation of the ZrO_2 from the M state to a mixture of T + C during fibre laser irradiation and from T + C to T followed by the M state during solidification. Variation between the TG-DSC curves for the as-received and fibre laser-treated ZrO_2 indicated that there was some level of chemical change within the fibre laser-treated ZrO_2 sample that allowed more mass flow to take place.

REFERENCES

1 **Cline, H. E.** and **Anthony, T. R.** Heat treating and melting materials with a scanning laser beam. *J. Appl. Phys.*, 1977, **48**, 3895–3900.

2 **Lax, M.** Temperature rise induced by a laser beam. *J. Appl. Phys.*, 1977, **48**, 3919–3924.

3 **Lax, M.** Temperature rise induced by a laser beam II. The nonlinear case. *J. Appl. Phys.*, 1978, **33**, 1127–1129.

4 **Nissim, Y. I., Lietoila, A., Gold, R. B.,** and **Gibons, J. F. R.** Temperature distributions produced in semiconductors by a scanning elliptical or circular CW laser beam. *J. Appl. Phys.*, 1980, **51**, 274–279.

5 **Moody, J. E.** and **Hendel, R. H.** Temperature profiles found by a scanning laser beam. *J. Appl. Phys.*, 1982, **53**, 4364–4371.

6 **Sanders, D. J.** Temperature distribution produced by a scanning Gaussian laser beam. *J. Appl. Opt.*, 1984, **23**, 30–35.

7 **Kar, A.** and **Mazumber, J.** Three-dimensional transient thermal analysis for laser chemical vapour deposition on uniformly moving finite slabs. *J. Appl. Phys.*, 1989, **65**, 2923–2934.

8 **Kar, A.** Effects of mode structure on three-dimensional laser heating due to single or multiple rectangular laser beams. *J. Appl. Phys.*, 1996, **80**, 667–674.

9 **Cheng, J.** and **Kar, A.** Mathematical model for laser densification of ceramic coating. *J. Mater. Sci.*, 1997, **32**, 6269–6278.

10 **Zhang, Z.** and **Modest, M. F.** Temperature dependent absorptances of ceramics for Nd:YAG and CO_2 laser processing applications. *J. heat Transf.*, 1998, **120**, 322–327.

11 **Hao, L.** and **Lawrence, J.** Numerical modeling of the laser surface processing of magnesia partially stabilized zirconia by the means of three-dimensional transient finite element analysis. *Proc. R. Soc. A*, 2006, **462**(2065), 43–57

12 **Ignatiev, M. B., Smurov, Y. I., Flamant, G.,** and **Senchenko, V. N.** Surface temperature measurement during pulsed laser action on metallic and ceramic materials. *J. Appl. Surf. Sci.*, 1996, **96–98**, 505–512.

13 **Braisted, W.** and **Brockman, R.** Finite element simulation of laser shock peening. *Int. J. Fatigue*, 1998, **21**, 719–724.

14 **Yongxiang, H., Zhenqiang, Y.,** and **Jun, H.** 3-D FEM simulation of laser shock processing. *Surf. Coat. Technol.*, 2006, **21**(3–4), 1426–1435.

15 **Ocana, J. L., Morales, M., Molpeceres, C.,** and **Torres, J.** Numerical simulation of surface deformation and residual stresses fields in laser shock processing experiments. *J. Appl. Surf. Sci.*, 2004, **238**, 224–248.

16 **Chen, H., Kysar, J. W.,** and **Lawrence, Y. Y.** Characterization of plastic deformation induced by micro-scale laser shock peening. *J. Appl. Mech. (ASME)*, 2004, **71**, 713–723.

17 **Kim, M. J.** 3-D Finite element analysis of evaporative laser cutting. *Appl. Math. Model.*, 2005, **29**, 938–954.

18 **Shiomi, M., Yoshidome, A., Abe, F.,** and **Osakada, K.** Finite element analysis of melting and solidifying processes in laser rapid prototyping of metallic powders. *Int. J. Mach. Tools Manuf.*, 1998, **39**, 237–252.

19 **Carmignani, C., Meres, R.,** and **Toselli, G.** Transient finite element analysis of deep penetration laser welding process in single pass butt-welded, thick steel plate. *Comput. Methods Appl. Mech. Eng.*, 1999, **179**, 197–214.

20 **Spina, R., Tricarico, L., Basile, G.,** and **Sibilano, T.** Thermo-mechanical modelling of laser welding of AA5083 sheets. *J. Mater. Process Technol.*, 2007, **191**, 215–219.

21 **Yilbas, B. S., Arif, A. F. M.,** and **Abdul Aleem, B. J.** Laser welding of low carbon steel and thermal stress analysis. *Opt. Laser Technol.*, 2009, **42**, 760–768.

22 **Zain-Ul-Abdein, M., Nélias, D., Jullien, J. F.,** and **Deloison, D.** Thermo-mechanical analysis of laser beam welding of thin plate with complex boundary conditions. *Int. J. Mater. Form.*, 2008, **1**, 1063–1066.

23 **Naeem, U. D., Qureshi, M. E.,** and **Hammouda, M.** Analysis of weld-induced residual stresses and distortions in Q12 thin-walled cylinders. *J. Mech. Sci. Technol.*, 2009, **23**, 1118–113.

24 **Zakurdaev, A.** and **Huang, X.** Experimental study of phase transformation and specific heat of ternary zirconia-based oxides using differential scanning calorimetry. *J. Alloys Compounds*, 2009, **488**, 469–478.

25 **Luping, L., Peigen, Z., Jiandong, L.,** and **Guo, S. M.** Phase transformation and morphological evolution of electrospun zirconia nanofibers during thermal annealing. *Ceram. Int.*, 2009, **36**, 589–594.

26 **Holand, W.** and **Beall, G.** *Glass–ceramic technology*, 2002 (The American Ceramic Society, USA).

27 **Garvie, R. C., Hannink, R. H.,** and **Pascoe, R. T.** The occurrence of metastable tetragonal zirconia as a crystallite size effect. *J. Phys. Chem.*, 1965, **69**(4), 1238–1243.

28 **Porter, D. L.** and **Heuer, A. H.** Mechanisms of toughening partially stabilized zirconia (PSZ). *J. Am. Ceram. Soc.*, 1977, **60**, 183.

29 **Sergio, M.** Thermal evaluation of ciria zirconia metallor- Q12 ganic precursors. *Thermochem. Acta* 1982, **58**, 253–25

30 **Zhou, Y., Ge, Q. L.,** and **Lei, T. C.** Microstructural and mechanical properties of $ZrO_2 - 2$, mol% Y_2O_3 ceramics. *Ceram. Int.*, 1990, **16**, 349–354.

31 **Sato, T.** and **Shimada, T.** Control of the tetragonal-to-monoclinic phase transformation of yttria partially stabilized zirconia in hot water. *J. Mater. Sci.*, 1985, 3988–3992.

32 **Haraguchi, K., Sugano, N., Nishi, T., Miki, H., Oka, K.,** and **Yoshikawa, H.** Phase transformation of a zirconia ceramic head after total hip arthroplasty. *J. Bone Joint Surg. (Br)*, 2001, **83-B**(7), 996–1000.

33 **Shackelford, J. F.** and **Doremus, H. R.** *Ceramic and glass materials (Structure properties and processing)*, 2008 (Springer Science + Bussiness Media, New York).

34 **Richardson, D. W.** *Modern ceramic engineering*, 3rd edition, 2006 (CRC Press, Taylor & Francis Group).

35 **Huang, X., Zakurdaev,** and **Wang, D. A.** Microstructure and phase transformation of zirconia-based ternary oxides from thermal barrier coating applications. *J. Mater. Sci.*, 2008, **43**, 2631–2641.

36 **Lee, W. L.** and **Rainforth, W. M.** *Ceramic microstructures*, 1994 (Chapman & Hall, London).

37 **Miao, X., Sun, D., Hoo, P., Woon, L., Jianli, H., Yifei,** and **Chen, Y.** Effect of Titania addition on yttria-stabilised tetragonal zirconia ceramics sintered at high temperatures. *Ceram. Int.*, 2004, **30**, 1041.

38 **Nayak, Y., Rana, R., Pratihar, S.,** and **Bhattacharyya, S.** Low-temperature processing of dense hydroxyapatite–zirconia composites. *Int. J. Appl. Ceram. Technol.*, 2008, **5**(1), 29–36.

39 **Sato, T., Ohtaki, S.,** and **Shimada, M.** Transformation of yttria partially stabilized zirconia by low temperature annealing in air. *J. Mater. Sci.*, 1985, **20**, 1466–1470.

40 **Zhu, W. Z.** Grain size dependence of the transformation temperature of tetragonal to monoclinic phase in ZrO_2 (Y_2O_3) ceramics. *Ceram. Int.*, 1996, **22**, 389.

41 **Sham, T.** NX 5.0 for designers. CADCIM Technologies, Purdue University Calumet, USA, 2007.

42 **Rolph, W. D.** and **Bathe, K. J.** An efficient algorithm for analysis of non-linear heat transfer with phase changes. *Int. J. Numer. Methods Eng.*, 1882, **18**, 119–134.

43 **Shukla, P. P.** and **Lawrence, J.** Characterization and compositional evaluation of Engineering ceramic. In Proceedings of the ICALEO 2009, Orlando, FL, 2009.

44 **Shukla, P. P., Lawrence, J.,** and **Wu, H.** On the fracture toughness of a zirconia engineering ceramic and the effects thereon of surface processing with fibre laser radiation. *Proc. IMecE, Part B: J. Engineering Manufacture*, 2009, **224**, (in press).

45 **Cengel, A. Y.** and **Turner, R. H.** *Fundamentals of thermal fluid sciences*, International edition, 2001 (Mc Graw Hill, Singapore).